THE ASTROPHYSICAL JOURNAL, 506:621–636, 1998 October 20

A VIEWING ANGLE–KINETIC LUMINOSITY UNIFICATION SCHEME FOR BL LACERTAE OBJECTS

MARKOS GEORGANOPOULOS AND ALAN P. MARSCHER
Department of Astronomy, Boston University, 725 Commonwealth Avenue, Boston, MA 02215
Received 1998 January 23; accepted 1998 May 28

ABSTRACT

We propose a unified classification for BL Lac objects (BLs), focusing on the synchrotron peak frequency ν_s of the spectral energy distribution. The unification scheme is based on the angle Θ that describes the orientation of the relativistic jet and on the electron kinetic luminosity $\Lambda_{\rm kin}$ of the jet. We assume that $\Lambda_{\rm kin}$ scales with the size of the jet r in a self-similar fashion ($\Lambda_{\rm kin} \propto r^2$), as supported by observational data. The jets are self-similar in geometry and have the same pressure and median magnetic field at the inlet, independent of size. The self-similarity is broken for the highest energy electrons, which radiate mainly at high frequencies, since for large sources they suffer more severe radiative energy losses over a given fraction of the jet length. We calculate the optically thin synchrotron spectrum using an accelerating inner jet model based on simple relativistic gasdynamics and show that it can fit the observed infrared–to–X-ray spectrum of PKS 2155−304. We couple the accelerating jet model to the unification scheme and compare the results to complete samples of BLs. The negative apparent evolution of X-ray–selected BLs is explained as a result of positive evolution of the jet electron kinetic luminosity $\Lambda_{\rm kin}$. We review observational arguments in favor of the existence of scaled-down accretion disks and broad emission-line regions in BLs. The proposed unification scheme can explain the lack of observed broad emission lines in X-ray–selected BLs, as well as the existence of those lines preferentially in luminous radio-selected BLs. Finally, we review observational arguments that suggest the extension of this unification scheme to all blazars.

Subject headings: BL Lacertae objects: general — galaxies: jets — radiation mechanisms: nonthermal

1. INTRODUCTION

The family of blazars includes those active galactic nuclei (AGNs) that are characterized by compact radio morphology and variable, polarized nonthermal continuum. Apparent superluminal motion and γ-ray emission are also common properties among blazars (for a review of their properties, see Urry & Padovani 1995). When the spectrum exhibits the usual quasar-like broad emission lines, the object is classified as a flat-spectrum radio quasar (FSRQ). On the other hand, the term "BL Lacertae object" ("BL") is reserved for the lineless or almost lineless blazars. The parent population of FSRQs (Padovani 1992) and BLs (Padovani & Urry 1990) is thought to consist of Fanaroff-Riley type II (FR II) and type I (FR I) radio galaxies (Fanaroff & Riley 1974), respectively.

The standard interpretation of the nonthermal continuum radiation of blazars from radio to γ-rays is synchrotron and inverse Compton emission from a collimated relativistic plasma jet (Blandford & Rees 1978). The currently popular paradigm involves the existence and dynamical consequences of a magnetic field that threads an accretion disk around a massive black hole (Blandford & Payne 1982). The collimation and acceleration of the jet in such a scenario is currently a field of active research; both analytical (see, e.g., Appl 1996) and numerical (see, e.g., Ouyed, Pudritz, & Stone 1997) work shows promising results thus far.

The observational taxonomy of BLs consists, according to the method of discovery, of radio-selected (RBLs) and X-ray–selected (XBLs) sources. According to Padovani & Giommi (1995), this corresponds to a more physical dichotomy, based on the frequency at which the peak of the synchrotron spectral energy distribution (SED, quantified by νL_ν) occurs: low-frequency–peaked BLs (LBLs), which are mostly RBLs, and high-frequency–peaked BL Lac objects (HBLs), which are mostly XBLs. The XBLs are less variable and polarized than RBLs (Jannuzi, Smith, & Elston 1994) and have flatter optical spectra (Ledden & O'Dell 1985). The RBLs are more core dominated (Perlman & Stocke 1993) and, for a given X-ray luminosity, are more luminous at radio and optical frequencies than XBLs (Maraschi et al. 1986). RBLs are characterized by a weak positive evolution (i.e., dependence of number counts on redshift; Stickel et al. 1991), while XBLs exhibit a negative evolution (Perlman et al. 1996). The recent discovery of a population of intermediate BLs (Laurent-Muehleisen 1997; Perlman et al. 1998) suggests a continuous family of objects rather than two separate classes.

Maraschi et al. (1986) proposed that the X-ray emission comes from a compact, less beamed region, while the radio emission comes from an extended, more beamed region. According to this "orientation hypothesis," the RBLs form a small angle ($\Theta \lesssim 10°$) between the line of sight and the direction of motion of the emitting plasma, while the XBLs form a larger angle ($10° \lesssim \Theta \lesssim 30°$). A more recent interpretation of the differences between XBLs and RBLs (Padovani & Giommi 1995) is based on the cutoff frequency of the synchrotron SED. According to this "SED-cutoff hypothesis," most of the BLs are characterized by a cutoff in the IR–optical band, and these are the radio-selected objects. The small fraction of BLs that have cutoffs at UV/X-ray energies are the X-ray–selected BL Lac objects. This model does not offer a physical explanation for the different cutoff frequencies of the SED.

There is an ongoing debate in the literature about the actual reason for the differences between XBLs and RBLs. Padovani & Giommi (1995) argue that the observed range of the core dominance parameter R (the ratio of core to extended radio flux) of the XBLs does not agree with the orientation hypothesis. On the other hand, Kollgaard et al.

(1996b) conclude that the fact that the mean core radio power of RBLs exceeds that of XBLs by more than an order of magnitude for sources selected according to extended radio power is incompatible with the SED-cutoff hypothesis. Comparison of VLBI images of RBLs and XBLs (Kollgaard, Gabuzda, & Feigelson 1996a) suggests that the jets in XBLs fade faster than those in RBLs, which supports the idea that factors other than orientation are also important in explaining the differences between XBLs and RBLs.

Urry & Padovani (1995) note that the SED-cutoff hypothesis cannot explain the different polarization properties of XBLs and RBLs, particularly the stability of the polarization angle in the XBLs. Lamer, Brunner, & Staubert (1996) analyze a sample of BL Lac objects observed with the Position Sensitive Proportional Counter (PSPC) detector on board the *ROSAT* satellite and note that the SED-cutoff hypothesis can explain the range of the cross-over frequency between the soft and the hard components in the X-ray regime better than the orientation hypothesis. Sambruna, Maraschi, & Urry (1996), using complete samples of BLs, reach the conclusion that the range of the peak frequency of the synchrotron energy distribution in BLs cannot be reproduced under the orientation hypothesis. An alternative scenario, which connects the synchrotron peak luminosity L_s to the synchrotron peak frequency ν_s of the SED of the BLs through an empirical relation, has been proposed recently by Fossati et al. (1997). One feature that this scenario reproduces more successfully than the previous two is the redshift distribution of XBLs and RBLs.

In this work, we propose that two parameters determine the observed characteristics of a BL. The first that must play a role, given the relativistic nature of the jet flow, is the angle Θ formed between the line of sight and the jet axis. The second is the electron kinetic luminosity $\Lambda_{\rm kin}$ of the jet. We start by developing and testing a numerical code for the accelerating inner jet model, which we use as our working hypothesis for the physical description of the jet. Invoking recent observational studies, we propose a new classification scheme, whose main observational parameter is the synchrotron peak frequency ν_s of the SED of BLs. We then introduce the theoretical Θ-Λ unification for BLs, based on two parameters: the angle Θ between the jet axis and the line of sight, and the electron kinetic luminosity $\Lambda_{\rm kin}$ of the jet. These are coupled to a simple self-similar jet description that relates $\Lambda_{\rm kin}$ to the size of the jet ($\Lambda_{\rm kin} \propto r^2$). We use the accelerating jet model to show how this unification scheme can be used to explain several characteristics of BLs, including the negative apparent evolution of the XBLs. We also show, using the self-similarity scenario we propose, that a picture in which BLs have scaled-down accretion disks and broad emission-line region (BELR) environments similar to those observed in FSRQs and high-polarization quasars (HPQs) is in agreement with observations. (We will use the terms FSRQ and HPQ interchangeably to signify all the non-BL blazars). Finally, we review observational evidence that supports a unified picture for all blazars under the above self-similar scheme.

2. THE JET MODEL

A first approach in calculating the synchrotron emission produced by an accelerating and collimating plasma flow was presented by Marscher (1980). In the accelerating inner jet model (based on the work of Blandford & Rees 1974 and Reynolds 1982), continuously generated ultrarelativistic plasma is confined by pressure (hydrostatic and/or magnetohydrodynamic) that decreases along the jet axis. The internal energy of the plasma is converted to bulk kinetic energy, and the jet is accelerated and focused. The electrons interact with a predominately random magnetic field and cool through synchrotron radiation and adiabatic expansion. At the same time, inverse Compton losses become important when the synchrotron photon energy density becomes comparable to the magnetic field energy density. Higher frequency radiation is emitted close to the base of the jet, since only there are the electron energies high enough to do so. Lower frequency photons are emitted there as well as farther downstream. The velocity of the jet increases with distance; this implies larger Doppler boosting for greater distances down the jet and therefore at lower frequencies, out to the point where the Lorentz factor $\Gamma \lesssim \Theta^{-1}$. The relevance of this approach to the BL Lac phenomenon was strengthened through studies that suggested that the X-ray–emitting region is less relativistically boosted than that of the radio emission (Maraschi et al. 1986; Urry, Padovani, & Stickel 1991).

We use the following phenomenological description for the accelerating inner jet. Ultrarelativistic plasma (mean ratio of total to rest mass energy per particle $\gamma \gg 1$ in the proper frame of the fluid) is continuously injected at the base of the jet. The bulk flow of the plasma at the injection point is parameterized by the bulk Lorentz factor $\Gamma_\star$. The axially symmetric pressure profile, with the pressure on the symmetry axis being less than the equatorial pressure, defines a preferred direction for the expansion of the plasma. The plasma flow is progressively accelerated and collimated, converting its internal energy to bulk kinetic energy. The adopted phenomenological description of ultrarelativistic particle injection at the base of the jet can be linked, for example, to particle acceleration in a standing shock front in the plasma flow, formed because of a drop in the confining pressure (Gómez et al. 1997). Since the emission at higher frequencies is confined to a region closer to the base of the jet than that at lower frequencies, we expect (Marscher 1980; Ghisellini & Maraschi 1989) shorter variability timescales at higher frequencies, given that the acceleration of the flow is mild. In addition, the Doppler effect is comparatively more important for the lower than for the higher frequencies. Therefore the jet orientation affects the lower frequencies more than the higher ones.

2.1. *Flow Description*

We adopt a flow description (see Appendix A) similar to that of Blandford & Rees (1974) and Marscher (1980), the latter of which considered as the base of the jet the sonic point, where the bulk Lorentz factor has the value $\Gamma_\star = (3/2)^{1/2}$. If we identify the base of the jet instead with a standing shock, we can relax the assumption that the flow is sonic at the base of the jet and allow for higher values of the bulk Lorentz factor $\Gamma_\star$ at that point. The minimum distance of the base of the jet from the accretion disk is obtained by requiring that the electron Thomson losses due to the accretion disk photons be less significant than the synchrotron losses (see Appendix B). The quantities that describe the flow are the total (electron + proton) kinetic luminosity Λ_t of the jet, the radius $r_\star$ of the base of the jet, and the exponent ϵ and the length scale $z_\star$ that describe how fast the jet opens and accelerates. Assuming energy equipartition between electrons and protons, the electron

kinetic luminosity $\Lambda_{\rm kin}$ is

$$\Lambda_{\rm kin} = \Lambda_t/2 \ . \tag{1}$$

Thus one-half of the injected energy is in protons that do not radiate, and therefore we can reasonably approximate the flow as adiabatic.

The bulk Lorentz factor as a function of distance along the jet axis is given by equation (A10),

$$\Gamma(z) = \Gamma_\star \left(\frac{z}{z_\star}\right)^{\epsilon} , \tag{2}$$

while the radius of the jet is given by a modified form of equation (A9):

$$r(z) = r_\star \left(\frac{z}{z_\star}\right)^{3\epsilon/2} (\Gamma_\star^2 - 1)^{1/4} \left[\Gamma_\star^2 \left(\frac{z}{z_\star}\right)^{2\epsilon} - 1\right]^{-1/4} . \tag{3}$$

For a three-dimensional steady flow, this equation applies to each streamline, but with $r(z)$ replaced by $r_{\rm str}$. The flow velocity is tangent to the streamlines and the loci of constant scalar quantities such as density are surfaces that are perpendicular to the streamlines. Note that, for $\Gamma_\star = (3/2)^{1/2}$, equation (3) is reduced to equation (A9).

2.2. *Magnetic Field*

For the purpose of this work, we will consider the magnetic field to be mainly random in direction, with a small ordered component parallel to the jet axis. Under the assumption of an isotropic electron distribution (see § 2.4), the choice of magnetic field geometry is not critical, since we are interested here in the total and not the polarized flux. Using simple flux conservation arguments, we assume that the magnetic field in the fluid frame decays as $B \propto r^{-m}$, $1 \le m \le 2$, or, in terms of the jet axial coordinate z,

$$B(z) = B_\star \left(\frac{z}{z_\star}\right)^{-3m\epsilon/2} (\Gamma_\star^2 - 1)^{-m/4} \times \left[\Gamma_\star^2 \left(\frac{z}{z_\star}\right)^{2\epsilon} - 1\right]^{m/4} . \tag{4}$$

2.3. *Electron Energy Losses*

We assume that the electrons are injected at the base of the jet and propagate downstream while losing energy because of adiabatic and synchrotron energy losses, without any reacceleration (except at downstream shocks fronts, the radiation from which is not considered here). The electrons will also suffer inverse Compton losses from the synchrotron photons they produce (the synchrotron self-Compton [SSC] model; see, e.g., Marscher & Bloom 1994) as well as from photons coming either from the broad-line clouds (Sikora, Begelman, & Rees 1994) or from the putative accretion disk (Dermer & Schlickeiser 1993) (external Compton [EC]). In our treatment we require that the base of the jet is sufficiently far from the central engine that the electron Thomson losses due to scattering of the accretion disk radiation are smaller than the synchrotron losses (see Appendix B). A self-consistent treatment of inverse Compton scattering is extremely complicated, since the local photon energy density results from photons that have been emitted in different regions of the jet at different retarded times. Observations using the *Compton Gamma Ray Observatory* (*CGRO*) (von Montigny et al. 1995; Dondi & Ghisellini 1995; Fossati et al. 1998) suggest that during flares the Compton luminosity is usually greater than the synchrotron in FSRQs by $\approx$1–2 orders of magnitude but is comparable to, or less than, the synchrotron luminosity in BLs, and during low states of γ-ray activity the synchrotron luminosity dominates the power output in BLs. In SSC models, the beaming cones of the synchrotron and Compton radiation are the same, and the ratio of the apparent luminosities of the two components equals the ratio of synchrotron to Compton electron losses.

In EC models, the beaming cone of the inverse Compton radiation is narrower than the synchrotron cone (Dermer 1995). Statistically, in the case of EC models, even if Compton losses are equal to the synchrotron losses, in any BL sample selected at frequencies dominated by synchrotron emission, one would expect that the Compton luminosity would be significantly greater than the synchrotron for a fraction of the sources equal to the ratio of the beaming-cone solid angles. Since this is not observed, it seems plausible to assume that the Compton losses even in EC-dominated BL models are not the main energy loss mechanism for BLs.

We combine the adiabatic and synchrotron losses to obtain the electron energy-loss equation in the fluid frame:

$$\frac{d\gamma(z)}{dz} = \left[\frac{d\gamma(z)}{dz}\right]_{\rm synch} + \left[\frac{d\gamma(z)}{dz}\right]_{\rm ad} = -C_1 \gamma^2 \left(\frac{z}{z_\star}\right)^{-3m\epsilon} (\Gamma_\star^2 - 1)^{-m/2} \times \left[\Gamma_\star^2 \left(\frac{z}{z_\star}\right)^{2\epsilon} - 1\right]^{(m-1)/2} - \frac{\epsilon\gamma}{z} , \tag{5}$$

where

$$C_1 = \left(\frac{2}{3}\right)^2 \frac{e^4}{m^3 c^6} B_\star^2 . \tag{6}$$

Since $(d\gamma/dz)_{\rm synch} \propto \gamma^2$ while $(d\gamma/dz)_{\rm ad} \propto \gamma$, synchrotron losses dominate for the higher energy electrons. The Lorentz factor γ describes the internal kinetic energy of the electrons in the fluid proper frame. Solving for the electron energy, we obtain

$$\gamma(z) = \left(\frac{z}{z_\star}\right)^{-\epsilon} \left[\frac{1}{\gamma(z_\star)} + C_1 (\Gamma_\star^2 - 1)^{-m/2} I(z)\right]^{-1} , \tag{7}$$

where the integral

$$I(z) = \int_{z_\star}^{z} \left(\frac{z}{z_\star}\right)^{-(3m+1)\epsilon} \left[\Gamma_\star^2 \left(\frac{z}{z_\star}\right)^{2\epsilon} - 1\right]^{(m-1)/2} dz \tag{8}$$

must be solved numerically for $m \neq 1$.

2.4. *Electron Energy Distribution*

The electron energy distribution (EED) is, in principle, determined by the particle acceleration and the dominant energy loss mechanisms acting simultaneously on the electrons (Kirk 1997). These two factors should determine the shape and the cutoffs of the distribution. In our model, we assume that the initially injected EED has a power-law form:

$$N(\gamma_\star, z_\star) = N_\star \gamma_\star^{-s}, \ \gamma_\star \in [\gamma_{\rm min}(z_\star), \gamma_{\rm max}(z_\star)] . \tag{9}$$

We further assume that the initial electron energy distribution (EED) remains isotropic in the comoving frame, through redistribution of the electron pitch angles due to their scattering on plasma waves. The EED distribution is therefore a function of energy and position along the jet axis only. The normalization factor $N_\star$ is related to the comoving energy density $e_{el\star}$ at the base of the jet,

$$e_{el\star} = \int_{\gamma_{\min}}^{\gamma_{\max}} \gamma N_\star \gamma^{-s}\, d\gamma = \frac{N_\star}{2-s}\,(\gamma_{\max}^{2-s} - \gamma_{\min}^{2-s})\,. \quad (10)$$

Using equation (A2) for the base of the jet ($A = r_\star^2$) and the relation $e_\star = (3/4)w_\star$ (see Appendix A), together with the assumed energy equipartition between electrons and protons ($e_{el\star} = e_\star/2$), we obtain

$$N_\star = \frac{3(2-s)\Lambda_{\rm kin}}{4\Gamma_\star^2 \beta_\star c(\gamma_{\max}^{2-s} - \gamma_{\min}^{2-s})}\,. \quad (11)$$

In our treatment it is implicitly assumed that the acceleration time is much shorter than the radiative loss time for the considered frequencies, and we can therefore separate the region where acceleration takes place from the radiative zone. This assumption may break down for the highest synchrotron frequencies, although, even in extreme objects like Mkn 421, the 1–10 keV variability behavior indicates that this assumption is valid (Kirk 1997). We therefore consider this approach adequate for synchrotron radiation with photon energy up to $\sim$10 keV. Conservation of particles and equation (7) give the evolved energy distribution:

$$N(\gamma, z) = N_\star \gamma^{-s}\left(\frac{z}{z_\star}\right)^{-\epsilon(s+2)} \times \left[1 - \gamma\left(\frac{z}{z_\star}\right)^{\epsilon} C_1(\Gamma_\star^2 - 1)^{-m/2} I(z)\right]^{s-2}\,. \quad (12)$$

This profile is no longer a power law, and on a log-log plot it gradually steepens toward higher frequencies. Note also that the EED evolves as the plasma moves downstream. This gives rise to a non–power law locally emitted synchrotron spectrum in the local flow frame, which changes with z in frequency cutoff and shape.

2.5. *Relativistic Transformations*

Given the magnetic field and the EED in the local fluid proper frame, we can calculate the synchrotron emission coefficient in the fluid frame using standard synchrotron formulae (Pacholczyk 1970):

$$\epsilon_\nu(z) = \frac{\sqrt{3}e^3}{4\pi mc^2}\, B(z)\, \sin\,\phi' \int_{\gamma_{\min}(z)}^{\gamma_{\max}(z)} N(\gamma, z) F(x)\, d\gamma\,, \quad (13)$$

where

$$F(x) = x \int_x^\infty K_{5/3}(z)\, dz\,. \quad (14)$$

$K_{5/3}$ is the modified Bessel function of order 5/3, and x is a dimensionless frequency:

$$x = \frac{\nu}{\nu_{\rm crit}(z)}\,,$$

where

$$\nu_{\rm crit}(z) = \frac{3e}{4\pi mc}\, B(z)\, \sin\,\phi'\, \gamma(z)^2\,.$$

In equation (13), ϕ' is the angle between the magnetic field and the line of sight in the fluid frame. In order to calculate this angle, we first need to transform the angle θ between the line of sight and the local flow velocity from the observer's frame to the fluid frame using standard relativistic aberration formulae (Rybicki & Lightman 1979):

$$\cos\,\theta' = \frac{\cos\,\theta - \beta}{1 - \beta\,\cos\,\theta}\,. \quad (15)$$

Having now the angle θ' between the line of sight and the local flow velocity in the local fluid frame, we can obtain ϕ' from the angle between the magnetic field and the local flow velocity in the fluid proper frame.

To transform the emission coefficient to the observer's (unprimed) frame we need to take into account the transformations between this frame and the fluid (primed) frame. If z is the redshift and $\delta = 1/[\gamma(1 - \beta\,\cos\,\theta)]$ is the Doppler boosting factor, where θ is the angle between the sight and the fluid velocity, then the frequency in the observer's frame is $\nu = \nu'\delta/(1+z)$ and the emission coefficient is (Rybicki & Lightman 1979)

$$\epsilon_\nu = \left(\frac{\delta}{1+z}\right)^2 \epsilon'_{\nu'}\,. \quad (16)$$

Having now obtained the synchrotron emission coefficient in the observer's frame, we can perform the radiative transfer and calculate the total synchrotron flux for optically thin frequencies.

3. MODEL SPECTRAL ENERGY DISTRIBUTIONS

3.1. *The Parameter Space*

We have performed an extensive study of the model parameter space in order to examine the response of the resultant SED to a variation of each physical parameter about the fiducial values given in Table 1. The meaning of the symbols is the same as in § 2. In Figure 1 we allow one of the model parameters to vary in each panel and plot the resulting SED.

As ϵ increases (corresponding to a more poorly collimated jet) the peak apparent synchrotron luminosity L_s decreases. This is because of an increase of the adiabatic losses and a decrease of the synchrotron power (cf. eq. [5]), regardless of the value of m. At the same time, the peak frequency ν_s of the SED increases, since the synchrotron losses decrease, and the effective break of the EED shifts to higher energies. An increase in the magnetic field amounts to an increase in L_s and a decrease in ν_s. This is expected since a higher magnetic field results in higher synchrotron

TABLE 1

MODEL PARAMETERS

Parameter	Value
$r_\star$ (cm)	10^{15}
$z_\star$ (cm)	2.0×10^{15}
$\Gamma_\star$	2.0
ϵ	0.3
$B_\star$ (G)	0.5
m	1.0
$\Lambda_{\rm kin}$ (ergs s^{-1}).....	10^{45}
$\gamma_{\min}$	10^2
$\gamma_{\max}$	2.0×10^5
s	2.0
Θ (deg)	10

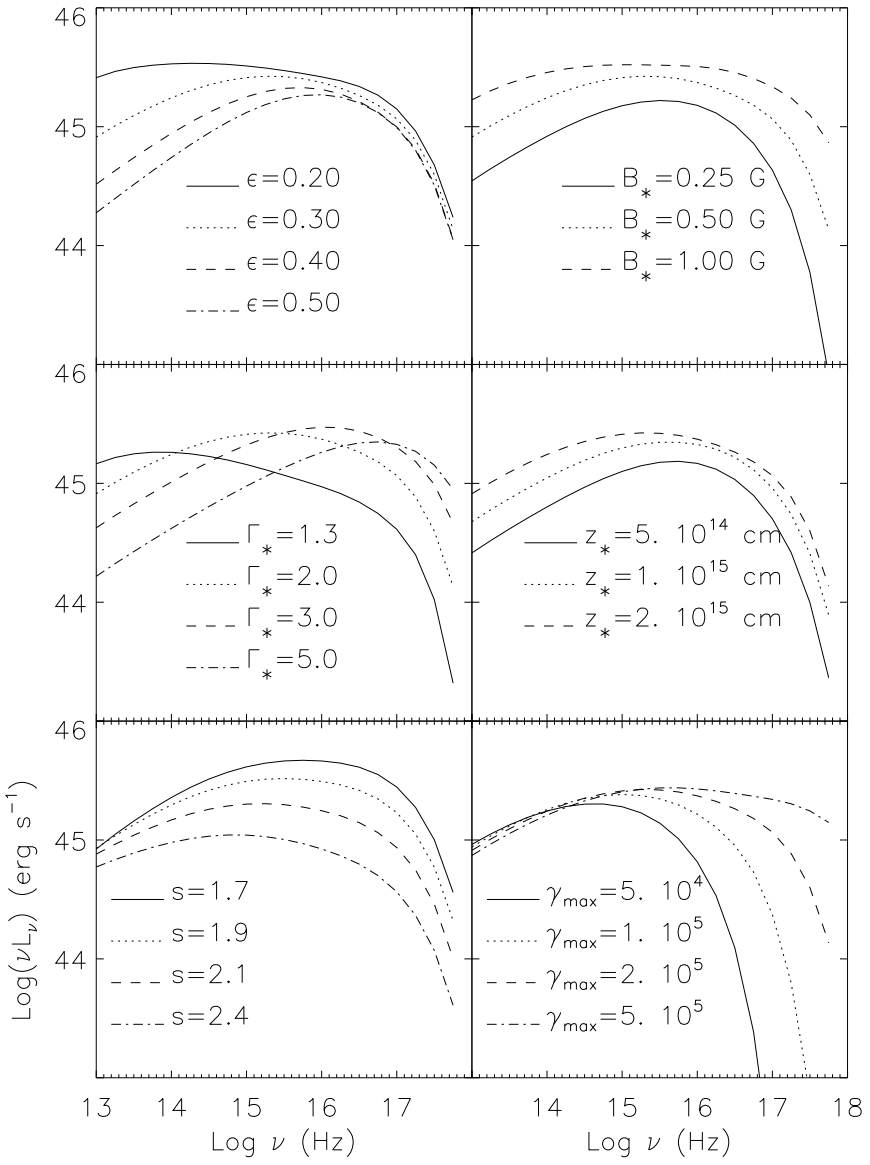

FIG. 1.—Model spectral energy distributions, for values of the parameters as given in Table 1, except for the single parameter allowed to vary in each panel. Here, L_ν is the apparent luminosity per unit frequency.

power and hence losses, primarily for the higher energy electrons.

The behavior of the SED as we increase $\Gamma_\star$ is less straightforward. As $\Gamma_\star$ increases, ν_s increases, the IR luminosity decreases, the X-ray luminosity increases, and L_s increases until $\Gamma_\star$ exceeds a critical value, beyond which it decreases. The key in understanding this behavior is that the jet emission is stratified, with the higher frequencies, which emerge closer to the base of the jet, being characterized by smaller Lorentz factors. As we increase $\Gamma_\star$, the effective Lorentz factor Γ_ν for each frequency increases, and the angle ($\approx 1/\Gamma_\nu$) into which the radiation is beamed decreases. In the IR regime (for the parameters chosen in Table 1), an increase in $\Gamma_\star$ beams most of the radiation into a cone with an opening angle smaller than Θ; this causes the Doppler deamplification we observe. In X-rays, the increase in $\Gamma_\star$ beams the radiation into a narrower cone that still includes the line of sight, and therefore the observed luminosity is more Doppler boosted. This frequency-dependent response causes ν_s to shift toward higher frequencies. L_s increases as long as the Doppler boosting of the higher frequencies can compensate for the Doppler deamplification at the lower frequencies. After a certain point (for the parameter values we use, this occurs at $\Gamma_\star \approx 3$), the observed peak luminosity declines, since most of the emitted power is beamed into a cone that does not include our line of sight.

An increase in $z_\star$ produces a behavior similar to that exhibited by the increase in $B_\star$. This is expected, since an increase in $z_\star$ causes the magnetic field to decline more slowly with time in the electron's frame. That is, the electron spends more time in the roughly uniform magnetic field region as the size of that region increases.

An increase in s (a steeper EED) produces a steeper spectrum, as expected. As the EED becomes steeper, the energy content of the high energy tail of the EED decreases. Since these are the electrons that lose energy faster and emit at higher frequencies, both L_s and ν_s decrease as the EED becomes steeper. An increase in the upper cutoff $\gamma_{\max}$ of the EED dramatically affects the high-frequency tail of the

SED, making the X-ray spectrum flatter and increasing both L_s and ν_s. The effect on the low frequencies is minimal, as expected, since the high-energy electrons radiate a small fraction of their power there. The behavior of the SED resembles that described by Padovani & Giommi (1995), who attribute the cause of the differences between XBLs and RBLs to different values of $\gamma_{\max}$.

The exponent m, which describes the evolution of the comoving magnetic field along the jet axis, and the radius of the jet $r_\star$ (not shown in Fig. 1) only weakly affect the SED. Increasing m from $m = 1$ to $m = 2$ decreases the IR luminosity by a factor of ~ 2, while the X-ray luminosity remains essentially the same. Increasing $r_\star$ by a factor of 4 reduces the X-ray luminosity by a factor of ~ 2, while the IR luminosity remains constant. Note, however, that in a time-dependent simulation the minimum variability timescale $[t_{\rm var} \gtrsim (r_\star \sin\Theta)/c]$ provides an upper limit to $r_\star$. The value of the lower cutoff $\gamma_{\min}$ of the EED should in principle be derived from the particle acceleration theory. For a given jet electron kinetic luminosity, as $\gamma_{\min}$ increases, the particle density and the observed synchrotron luminosity increase, since the average energy per particle increases. Hence, $\Lambda_{\rm kin}$ and $\gamma_{\min}$ are closely connected and only one ($\Lambda_{\rm kin}$) needs to be treated as a free parameter unless the value of the density is needed. For the purpose of this work we will assign the values $m = 1$ and $\gamma_{\min} = 10^2$.

For a given physical description of the jet, the angle Θ between the jet axis and the line of sight is still a free parameter, in the sense that the jet can be oriented at any angle relative to the line of sight. As mentioned in the introduction, one of the leading scenarios for the interpretation of the differences between RBLs and XBLs is based on the orientation of the jet relative to the line of sight. We have run our simulation using the parameters of Table 1 and have allowed the angle to vary, as presented in Figure 2. The data points refer to the 1 Jy sample of RBLs (*triangles*) and the *Einstein* Extended Medium Sensitivity Survey sample of XBLs used by Sambruna et al. (1996). As can be seen in the bottom panel, as the angle increases from $\Theta = 0°$ to $\Theta = 20°$, the synchrotron luminosity L_s decreases by a factor of ~ 20 and the synchrotron peak frequency ν_s increases by ~ 2 orders of magnitude. At the same time the spectrum becomes flatter at all frequencies. The synchrotron peak luminosity L_s (*middle panel*) and the optical–to–X-ray spectral index $a_{\rm ox}$ (*top panel*), calculated taking into account the luminosities at 5500 Å and at 1 keV, are plotted versus the peak frequency ν_s of the SED. Note that the model point shifts from a predominately RBL region to a predominately XBL region in both the luminosity and spectral index plots as the angle increases. This behavior is not specific to the set of model parameters used here but appears in a qualitatively similar manner for a wide range of initial conditions: as the angle increases, L_s decreases, ν_s increases, and the spectrum becomes flatter. Although these differences are similar to the differences found between XBLs and RBLs, previous work (Sambruna et al. 1996; Georganopoulos & Marscher 1996) has shown that a change in only the jet orientation is not enough to explain the range of observed properties of BLs; hence additional physical differences must be invoked.

3.2. *Simulation of the SED of PKS 2155−304*

As an application of the model, we simulate the SED of PKS 2155−304, a relatively nearby (redshift $Z = 0.116$)

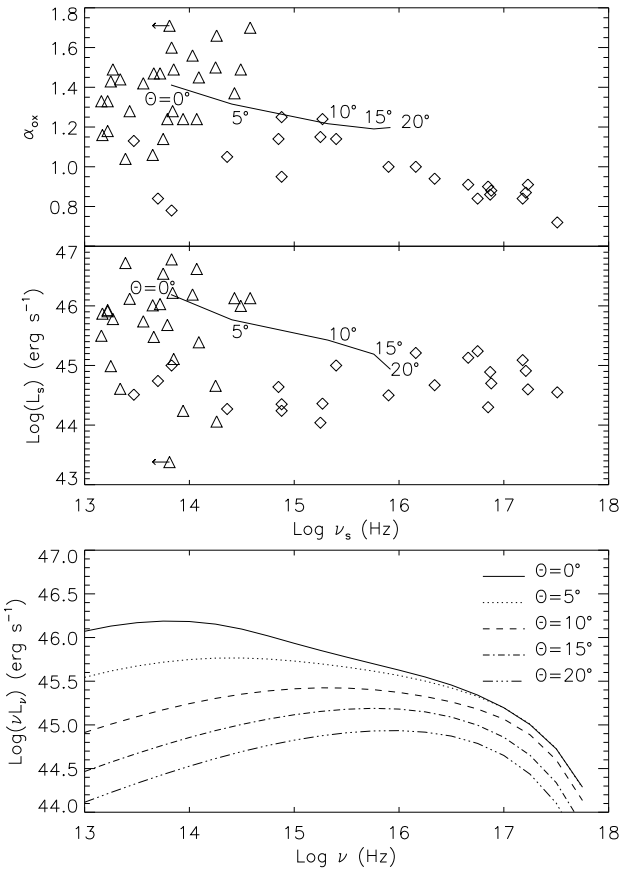

FIG. 2.—*Bottom panel*: SEDs for values of the parameters given in Table 1, for various observing angles Θ between the jet axis and the line of sight. Peak luminosity L_s (*middle panel*) and optical to X-ray spectral index $\alpha_{\rm ox}$ (*top panel*) versus observed peak synchrotron frequency ν_s. The data points correspond to samples of RBLs (*triangles*) and XBLs (*diamonds*) (Sambruna, Maraschi, & Urry 1996), and the curves correspond to the model.

bright XBL. Its γ-ray luminosity is less than its synchrotron (Vestrand, Stacy, & Sreekumar 1995), which implies (see also § 2.3) that synchrotron losses are more important than inverse Compton losses. The object has been the target of two intensive multiwavelength campaigns, one during 1991 November (Edelson et al. 1995), and one during 1994 May (Urry et al. 1997).

Since PKS 2155−304 is highly variable, and a strictly simultaneous SED is practically unattainable, we must approximate a simultaneous SED with one constructed from fluxes measured during a time interval smaller or at least comparable to the timescale of the fastest significant variations. The shortest variability timescale for the 1991 November data set was ≈ 0.7 days. We construct the SED plotted in Figure 3 using observations in the time interval between November 14.0 and 14.76. This time interval is approximately equal to the fastest variability timescale observed, and it corresponds to a local flux minimum for the optical–to–X-ray frequency range. The solid curve in Figure 3 represents the best-fit model. The values of the parameters used are given in Table 2. The χ^2 for this fit is 49.65 for 9 degrees of freedom. This high value can be partly attributed to the arbitrariness of the selected observed fluxes used to construct the "base" observed SED but in any case is typical of fits to multiwavelength spectra with noncomplex models. Since an exhaustive exploration of the

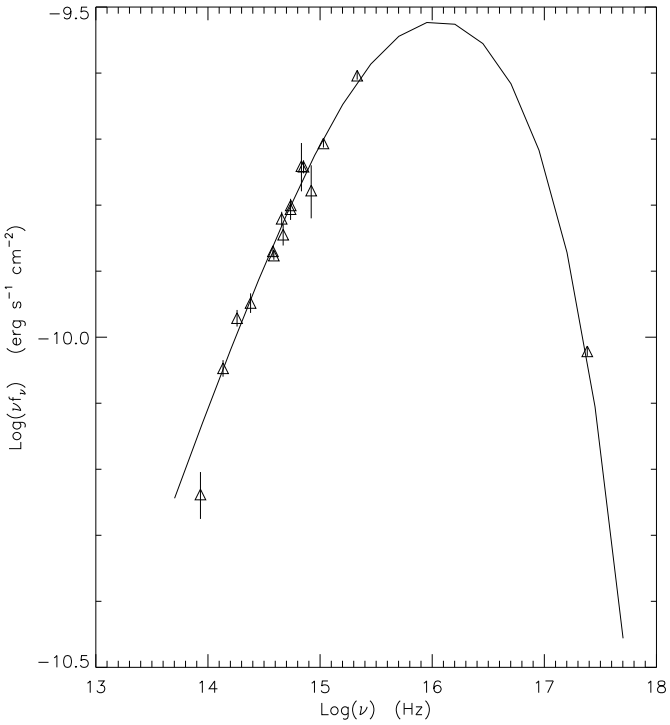

FIG. 3.—Spectrum of PKS 2155−304 during the multiwavelength campaign of 1991 November. The data were obtained on November 14 during an 18 hr period. (Edelson et al. 1995). The solid curve corresponds to the model fit produced using the parameters listed in Table 2.

parameter space is practically impossible, we cannot assert that this is the best possible fit. To derive a more constrained description of the source, we would need to model successfully the observed variability behavior.

4. A NEW SED-BASED CLASSIFICATION SCHEME

BL Lac objects are discovered mostly through X-ray or radio surveys. The existing complete samples therefore are either X-ray– (Morris et al. 1991; Perlman et al. 1996) or radio flux–limited samples (Stickel et al. 1991), and BLs are named XBL (X-ray–selected) or RBL (radio-selected) depending on the method of discovery. In general, RBLs have steeper spectra than do XBLs. The SEDs of RBLs peak somewhere in the infrared and have higher synchrotron peak luminosities L_s than do the XBLs, which usually peak in the UV–soft X-ray range (Sambruna et al. 1996).

A recently proposed classification scheme for BLs (Padovani, Giommi, & Fiore 1996) corresponds more closely to the observed characteristics of the objects than the method of discovery. According to this scheme, BLs are classified as high frequency–peak BLs (HBLs) or low frequency–peak BLs (LBLs), depending on the value of the X-ray to radio flux ratio. Objects with $f_X/f_r \lesssim 10^{-11.5}$ are classified as LBLs and objects with $f_X/f_r \gtrsim 10^{-11.5}$ as HBLs. Most of the HBLs are XBLs and most of the LBLs are RBLs. Although this classification scheme is based on observed properties of BLs, it inherits the dichotomization of BL Lac objects that was imposed by the two different discovery methods. Such a dichotomization can hinder our efforts to understand the physics of BLs, particularly if the two methods of discovery force us to observe the two extremes of a continuous distribution, thereby introducing a selection-induced bimodality.

TABLE 2

MODEL PARAMETERS FOR PKS 2155−304

Parameter	Value
$r_\star$ (cm)	1.1×10^{15}
$z_\star$ (cm)	1.5×10^{15}
$\Gamma_\star$	1.5
ϵ	0.3
$B_\star$ (G)	0.11
Λ_{kin} (ergs s^{-1})	8.63×10^{45}
γ_{max}	6.5×10^5
s	1.7
Θ (deg)	10

Strong indications that a bimodality is introduced by the observational techniques come from a recent study by Laurent-Muehleisen (1997). The cross-correlation of the *ROSAT* All Sky Survey (RASS) and the Green Bank 5 GHz radio survey revealed the existence of a previously highly undersampled population of BLs (120 objects) with properties intermediate between those of XBLs and RBLs. Specifically, the X-ray to radio flux ratio of these sources and their location on a diagram of radio-to-optical (α_{ro}) versus optical–to–X-ray (α_{ox}) spectral indeces bridge the gap between XBLs and RBLs. Similar results (Perlman et al. 1998) are emerging from the deep X-ray radio blazar survey (DXRBS). The question that naturally arises is whether there is an observed quantity that varies in a continuous fashion, has a well-defined physical significance, and can be used as a classifying parameter. We argue that such a quantity is the synchrotron peak frequency ν_s.

Recently, Sambruna et al. (1996) examined the multifrequency spectral properties of three complete samples of blazars: the *Einstein* Extended Medium Sensitivity Survey sample (EMSS) of XBLs (23 sources; Morris et al. 1991), the 1 Jy sample of RBLs (29 sources; Stickel et al. 1991), and a small complete sample of FSRQ from the S5 survey (eight sources; Brunner et al. 1994). After they calculated the rest frame fluxes and spectral indices for each object, they fit a parabola to the synchrotron power (νL_ν) spectrum. X-ray fluxes were excluded from the fitting in the cases in which the X-ray spectral index α_X was flatter than the broadband optical to X-ray spectral index α_{ox}, a condition that is thought to indicate that inverse Compton radiation dominates over the steep high-energy synchrotron tail of the spectrum. In Figure 4*a*–4*f*, we plot the spectral indices α_{ox}, α_{ro}, α_{rx}, the X-ray concavity index $\alpha_{ox} - \alpha_X$, and the synchrotron bolometric L_B and peak L_s luminosities as functions of the synchrotron peak frequency ν_s for the two BL samples of Sambruna et al. (1996). If we consider the two samples collectively, we find that each of the six diagrams there is an upper envelope separating the populated area from a well-defined zone of avoidance. The upper envelope is such that for a given peak frequency ν_s there is a range of "avoided" luminosities and spectral indices. As ν_s increases, the maximum observed luminosity decreases, the steepest observed spectral index flattens, and the maximum observed concavity index $\alpha_{ox} - \alpha_X$ decreases. On the other hand, the flattest spectral indices observed and the most negative concavity indices do not seem to be very sensitive to the value of ν_s.

We propose a continuous classification system for BLs, based on the synchrotron peak frequency ν_s of the synchrotron SED. For example, a BL peaking at log $\nu_s \approx 14$ will be classified as a BL14. The class of a BL Lac object then

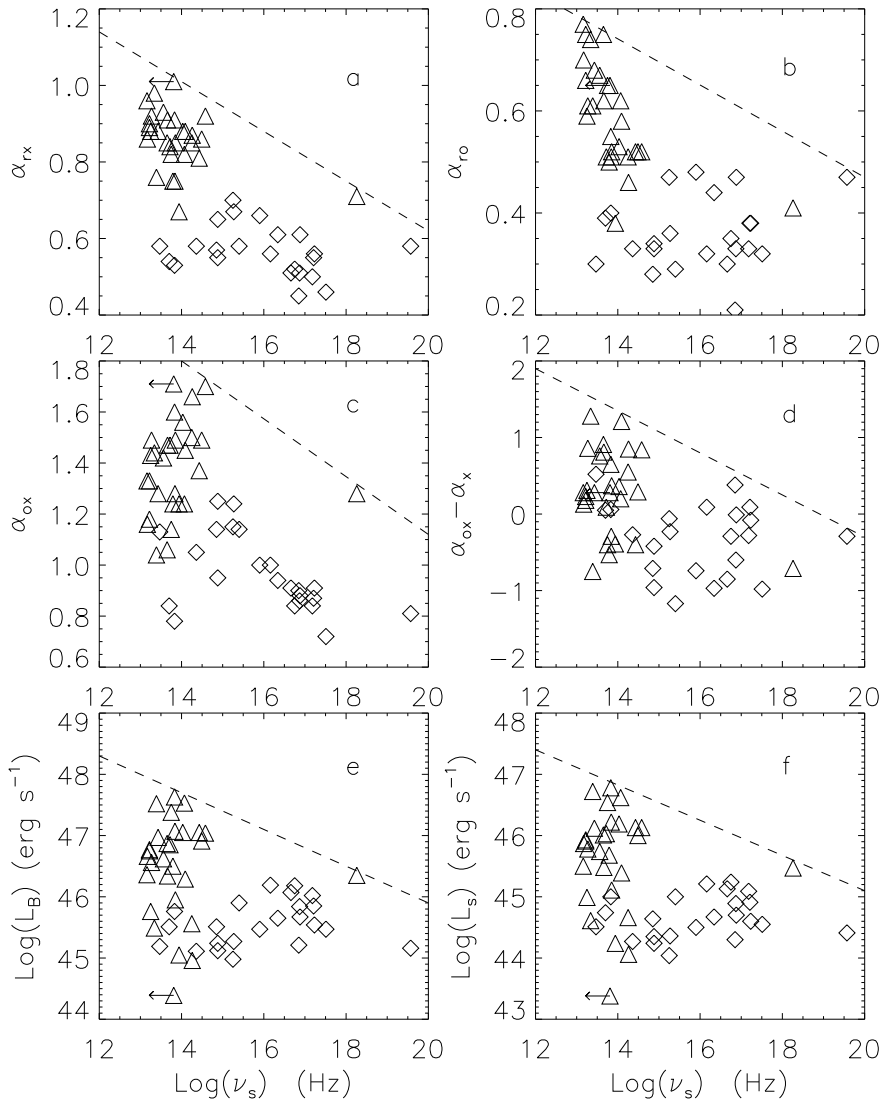

FIG. 4.—(*a*) Radio to X-ray (α_{rx}), (*b*) radio to optical (α_{ro}), and (*c*) optical to X-ray (α_{ox}) broadband spectral indices; (*d*) the X-ray concavity index $\alpha_{ox} - \alpha_X$; (*e*) the bolometric synchrotron apparent luminosity L_B; and (*f*) the synchrotron peak luminosity L_s, as a function of the observed synchrotron peak frequency ν_s of the synchrotron power spectrum for the XBL (*diamonds*) and RBL (*triangles*) samples of Sambruna et al. (1996). The arrows indicate an RBL with only an upper limit to the peak frequency ν_s. The dashed lines separate the populated from the unpopulated areas of the diagrams.

defines the maximum luminosity of the object, the maximum steepness of its synchrotron spectrum over a range of frequencies, and the maximum concavity index. We note here that (unlike the transient variability mentioned before) long-term, persistent changes in ν_s, should be reflected in the classification of the object.

The synchrotron peak frequency ν_s of a BL is a very important parameter from a physical point of view as well. It is the frequency in which we receive the highest synchrotron power per logarithmic frequency interval. It is also closely related to the peak of the inverse Compton emission in both the SSC (Bloom & Marscher 1996) and the EC models (Sikora, Begelman, & Rees 1994; Dermer & Schlickeiser 1993). This frequency is closely linked to the energetics and geometry of the synchrotron source and to the angle formed between the observer and the plasma velocity, if the source is moving relativistically (see § 3).

As Sambruna et al. (1996) point out, the determination of ν_s requires simultaneous multiwavelength flux measurements and can be particularly sensitive to a lack of flux measurements close to the peak of the distribution. The problem of multiwavelength coverage becomes more difficult when ν_s happens to be either in the observationally inaccessible frequency range between submillimeter and infrared frequencies $\nu \approx 10^{12}$–10^{14} Hz or in the UV because of Galactic absorption. If ν_s is in the X-ray energy range, and there are no flux measurements to constrain the parabola at frequencies higher than ν_s, the error in ν_s can be very large. This is the case for the two sources that have $\log \nu_s > 18$, the XBL 1433.5+6369 and the RBL 2005−489 (see Fig. 4 of Sambruna et al. 1996), which we decided not to consider further in our study. In general, the error in the determination of ν_s should be smaller for objects with SEDs peaking at IR–optical frequencies, where ν_s is more easily constrained.

We note, however, that even though ν_s is difficult to measure exactly, an approximate estimate within a decade of frequency is both feasible and adequate for the purpose of classification. Furthermore, the accuracy can be improved if one decides to perform multiwavelength observations with

this specific goal in mind, instead of using the available data from the literature.

Variability can also affect ν_s. In the case of individual flares, initially the spectrum hardens (Ulrich, Maraschi, & Urry 1997) and the peak synchrotron frequency increases. This change is temporary, and the source returns to its preflare characteristics after the end of the flare. The most extreme recorded case of such a shift occurred in Mkn 501, which increased its synchrotron peak frequency by more than a factor of 100, changing from a BL17 to a BL19 (Pian et al. 1998). Usually, though, the shift in ν_s, something neither easily nor customarily calculated in multi-wavelength studies, is approximately a factor of 10 in the case of the few well documented, large amplitude flares. In the case of Mkn 421 during the 1994 May (Macomb et al. 1995) and the 1995 April–May (Buckley et al. 1996) campaigns, ν_s increased by a factor $\approx$10–100, while during the PKS 2155−304 1994 May campaign, ν_s increased by less than a factor of 10 (Urry et al. 1997). Since these excursions of ν_s are usually of the same magnitude as the uncertainty in measuring ν_s, and also of a transient character, we do not consider them a serious problem in assigning a specific ν_s to a BL, regardless of variability.

Under our proposed unified classification based on ν_s, the questions that can direct us toward a physical unification are: (1) which are the physical and/or geometrical parameters that, given their range of values, create the range of the observed phenomenology?, and (2) can a model incorporate these parameters and derive the properties of complete samples of BL Lac objects? In the following section, we propose a simple unification scheme based on a self-similar jet description.

5. A Θ-Λ UNIFICATION SCHEME

5.1. *A Self-Similarity Hypothesis*

In order to the extended region that BLs occupy in the diagrams of Figure 4, we need to employ a model with at least two free parameters. Any model with only one free parameter can at best trace a curved trajectory in the observational graphs when this free parameter is allowed to vary. Under the assumption that the jets of BLs are relativistic, a change in the angle between the line of sight and the jet axis will induce a model-dependent change in the observed properties of the source. It therefore seems necessary to postulate minimally the existence of a physical free parameter that, together with the angle, is capable of reproducing the observed range of properties of BLs.

The concept that relativistic jets can be described in a scale-invariant way using a self-similar description is very appealing, since these physical configurations span a luminosity range greater than 10 orders of magnitude, from the jets in stellar systems in our Galaxy to the most extreme FSRQs. Maraschi & Rovetti (1994), after studying samples of BLs, FSRQ, and FR I and FR II radio galaxies, suggested that all these sources operate in a self similar way, with the jet luminosity and angle between the line of sight and the jet axis accounting for the different observed properties. Gear (1993) studied the infrared colors of two complete samples of RBLs and XBLs and hinted toward a BL unification based on the luminosity and the angle between the line of sight and the jet axis.

We propose that the second physical unification parameter is the electron kinetic luminosity of the jet, $\Lambda_{\rm kin}$. At first view, one would be tempted to assume that $\Lambda_{\rm kin} \propto r_\star$, since the Eddington luminosity scales with the black hole mass, which is proportional to the gravitational radius of the black hole. However, tying the luminosity of the system to the black hole mass cannot address the evolutionary characteristics of BLs. The black hole mass slowly increases, because of accretion of fresh material, and this translates into a slow increase of the luminosity, which essentially translates to a weak negative cosmological evolution, i.e., each source becomes more powerful as cosmic time increases. We know that this is the case neither for RBLs (see § 5.3), nor for all the other radio-loud AGN families (Urry, & Padovani 1995), which we presume are described by the same paradigm—a massive black hole, an accretion disc, and a relativistic jet.

An alternative description has been proposed by Rees et al. (1982). Under this scheme, the electromagnetic power $L_{\rm EM}$ extracted from of a rapidly rotating black hole is proportional to a^2, where $a < r_g$ is a length that measures the specific angular momentum ac of the black hole, and r_g is the gravitational radius of the black hole. Assuming now that $L_{\rm EM}$ and a are related linearly to $\Lambda_{\rm kin}$ and $r_\star$ correspondingly, we propose that $\Lambda_{\rm kin}$ scales as $r_\star^2$

$$\Lambda_{\rm kin} \propto r_\star^2 \,. \tag{17}$$

Under this scheme, the main cause for evolution is the spin-down of the black hole, manifested as a decrease of a due to the continuous energy extraction. This way the power of the source decreases with cosmic time, giving rise to the observed positive cosmological evolution, in the sense that sources were more powerful in the past (the apparent negative evolution of XBLs is addressed in § 5.3).

We additionally assume that the intensive physical variables that describe the relativistic jet in BLs, such as the magnetic field, the comoving plasma density, and the high-energy cutoff of the injected electron energy distribution, all vary over a small intrinsic range of values. The combination of these two assumptions suggests a unification scheme in which the observed properties of a BL depend mainly on the electron kinetic luminosity $\Lambda_{\rm kin}$ of the jet and the angle between the line of sight and the jet axis Θ. A similar scaling relation has been discovered observationally between the size $R_{\rm BELR}$ of the broad emission-line region (BELR) and the central (accretion disk) ionizing luminosity $L_{\rm acc}$ of Seyfert galaxies and quasars (Kaspi et al. 1996) using reverberation mapping:

$$L_{\rm acc} \propto R_{\rm BELR}^2 \,. \tag{18}$$

This scaling law implies an ionization parameter U (ratio of ionizing photon density to electron density) that has a small intrinsic range of values ($U \sim 0.1$–1) for objects that extend in luminosity over almost 4 orders of magnitude (Wandel 1998). Observational arguments, suggestive of a self-similar description of radio-loud AGNs, have been presented by Rawlings & Saunders (1991), who find that the kinetic luminosity of the kiloparsec-scale jet is proportional to the narrow emission line luminosity. This relation holds for objects with or without broad emission lines and extends for more than 4 orders of magnitude in luminosity. In a similar study, Celotti, Padovani, & Ghisellini (1997) find that $L_{\rm BELR}$ and the parsec-scale kinetic luminosity of the jet for a sample of radio loud AGNs are of the same order of magnitude. As recent studies of radio loud AGNs suggest (see, e.g., Koratkar et al. 1998), the BELR is probably

ionized by thermal radiation from the central engine, rather than by the jet radiation.

We adopt as a working hypothesis a picture in which the ionizing luminosity of the accretion disk $L_{\rm acc}$, the jet electron kinetic luminosity $\Lambda_{\rm kin}$, and the BELR luminosity $L_{\rm BELR}$ are closely related, scaling as

$$L_{\rm acc} \propto L_{\rm BELR} \propto \Lambda_{\rm kin} \propto r_\star^2 , \qquad (19)$$

where $r_\star$ is a dimension that characterizes the jet. We stress here that this scaling assumption does not refer to a specific jet model but is a rather general, model-independent hypothesis that can be applied to specific jet models.

5.2. *Application to the Accelerating Jet Model*

We apply this self-similar scheme to the accelerating jet model. The question we address here is whether we can populate the ν_s-L_s diagram of Figure 4*f*, under the assumptions that the jet electron kinetic luminosity scales with the square of the jet size, and that the physical parameters that describe the jet have a small intrinsic range of values. We perform calculations using two somewhat different families of values for the physical parameters, listed in Table 3. For each family, we run the simulation for a range of angles and luminosities, scaling the square of $r_\star$ and $z_\star$ with the electron kinetic luminosity $\Lambda_{\rm kin}$. The results of this set of simulations can be seen in Figure 5. The solid curves represent calculated values of L_s for a constant electron kinetic luminosity and size as the angle Θ varies between 0° and 18°. The dot-dashed curves correspond to constant angle as the electron kinetic luminosity $\Lambda_{\rm kin}$ increases from Λ to 256Λ, where $\Lambda = 10^{43}$ ergs s^{-1}. This increase in luminosity is accompanied by an increase in the jet size: $r_\star$ and $z_\star$ increase by a factor of 16, starting at $r_\star = 2.5 \times 10^{14}$ cm and $z_\star = 5.0 \times 10^{14}$ cm.

The qualitative behavior of both model families is the same. For a given electron kinetic luminosity, as the angle Θ increases, the peak frequency ν_s increases and the peak apparent luminosity L_s decreases. For a constant angle, as $\Lambda_{\rm kin}$ decreases, there is a drastic decrease in L_s and a milder increase in ν_s. The two families of models generated by these somewhat different physical descriptions cover a significant portion of the observed range of values. This behavior is not specific to the above choice for the physical parameters: a different set of jet parameters would generate a pattern similar to those obtained by the models of Figure 5 and Table 3. Modest changes in the physical description merely move the grid around the observed parameter space. A small range of values for the physical description of the jet, coupled with the Θ-Λ scheme, can populate the ν_s-L_s diagram for BLs. Choosing the appropriate set of jet parameters, the Θ-Λ scheme can produce synthetic spectra of BL18–BL19 sources. We choose not to do so, since the determination of ν_s for the two sources with $\log \nu_s \geq 18$ in Sambruna et al. (1996) is problematic.

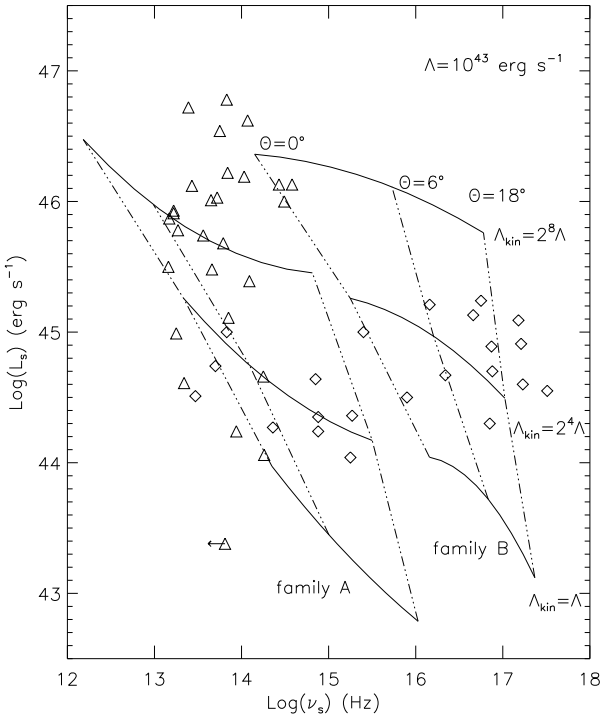

FIG. 5.—Synchrotron apparent peak luminosity L_s as a function of the observed synchrotron peak frequency ν_s of the SED for the XBL (*diamonds*) and RBL (*triangles*) samples of Sambruna et al. (1996). The two superposed grids are the results of the accelerating jet model coupled with the scaling assumption of eq. (19) for two different physical descriptions of the jet, as given in Table 3. The solid curves represent constant electron kinetic luminosity $\Lambda_{\rm kin}$, while the dot-dashed curves correspond to a constant angle Θ between the jet axis and the line of sight.

TABLE 3

VALUES OF PARAMETERS USED IN SIMULATIONS UNDER THE Θ-Λ SCHEME (SEE FIG. 5)

Parameter	Family A	Family B
$r_\star$	$r^{\rm a}$, 2^2r, 2^4r	$r^{\rm a}$, 2^2r, 2^4r
$z_\star$	$z^{\rm b}$, 2^2z, 2^4z	$z^{\rm b}$, 2^2z, 2^4z
$\Gamma_\star$	1.5	2.0
ϵ.....	0.3	0.4
$B_\star$ (G).....	0.4	0.4
$\Lambda_{\rm kin}$	$\Lambda^{\rm c}$, $2^4\Lambda$, $2^8\Lambda$	$\Lambda^{\rm c}$, $2^4\Lambda$, $2^8\Lambda$
$\gamma_{\rm max}$	4×10^5	8×10^5
s.....	2.0	1.7

[a] $r = 2.5 \times 10^{14}$ cm.
[b] $z = 5.0 \times 10^{14}$ cm.
[c] $\Lambda = 10^{43}$ ergs s^{-1}.

The conclusion reached previously by Sambruna et al. (1996) and Georganopoulos & Marscher (1996) that the range of ν_s cannot be explained merely by jet orientation is supported by this study. However, a combination of jet orientation and a relatively small range in the physical parameters that describe the jet can explain the range of ν_s under the Θ-Λ scheme. A quantitative comparison, including specific assumptions about the range of the physical parameters and extensive comparison of synthetic samples to existing samples, does not seem worthwhile until the parameters can be more strictly constrained, for example through analyses of multiwavelength variability.

One might naively expect that, for a given angle, since the jet electron kinetic luminosity and size scale in a self-similar fashion, the SED would follow this self-similar behavior by scaling up or down, following the electron kinetic luminosity and keeping its shape and peak frequency the same. An important feature emerging from our simulations is that for a constant angle, as the electron kinetic luminosity and the size of the jet increase, the peak frequency decreases. This means that, although the jet scales in a self-similar manner, this self-similarity is not transferred completely to the SED, since the peak frequency changes. The reason for

this break-down is that the effects of synchrotron losses (cf. eq. [12] and the discussion in § 3.1) on ν_s do not follow scaling laws that are qualitatively similar to those that govern the behavior of L_ν at $\nu \leq \nu_s$. For example, if the values of $r_\star$ and $z_\star$ were doubled while holding $B_\star$ constant, ν_s would decrease because the electrons would suffer more severe synchrotron losses as they traverse the characteristic distance $z_\star$ before encountering the region of the jet where B decreases.

5.3. *The Negative Evolution of XBLs*

The evolution of all the AGN families is positive, in the sense that these objects were either more common or more luminous (or both) in the past. A unique and striking exception is the negative evolution of XBLs: Morris et al. (1991) showed that the evolution of the EMSS XBL sample is negative. It seems that these objects were either less common or less luminous in the past. This has been verified recently by Perlman et al. (1996) for the *ROSAT* PSPC sample of XBLs, with $\langle V_e/V_a \rangle = 0.331 \pm 0.060$, where V_e is the volume of a sphere with radius equal to the distance to each object and V_a is the available volume within which each object could have been detected in the EMSS. This result is in contrast to the value $\langle V_e/V_a \rangle = 0.60 \pm 0.05$ obtained by Stickel et al. (1991) for the 1 Jy RBL sample.

This negative evolution of XBLs can be explained naturally in the framework of the Θ-Λ scheme, under the assumption commonly invoked for AGNs that the electron kinetic luminosity $\Lambda_{\rm kin}$ of the radio-loud AGN jets has a positive evolution; viz., jets (on average) in AGNs had a higher $\Lambda_{\rm kin}$ in the past. As we showed in § 5.2 for a given set of physical parameters and angle Θ, as $\Lambda_{\rm kin}$ decreases, the peak synchrotron apparent luminosity L_s decreases and the peak synchrotron frequency ν_s increases, essentially shifting the source from the region of the RBL-type objects toward that of the XBL-type objects. If we start with a sample of sources characterized by a range of $\Lambda_{\rm kin}$ and Θ and let these sources evolve to lower values of electron kinetic luminosity $\Lambda_{\rm kin}$, then each source will gradually (with cosmological time) shift its characteristics to become more XBL-like. This means that the fraction of sources that would be classified as RBLs will gradually decrease with time/redshift, resulting in $\langle V_e/V_a \rangle \gtrsim 0.5$ in a radio flux–limited sample, while the fraction of sources that would be classified as XBLs will gradually decrease and yield $\langle V_e/V_a \rangle \lesssim 0.5$ in an X-ray flux–limited sample.

Our model predicts that the value of $\langle V_e/V_a \rangle$ of an intermediate BL sample, such as that of Laurent-Muehleisen (1997), will be confined between the corresponding values of $\langle V_e/V_a \rangle$ for the XBL and RBL samples mentioned above, exhibiting almost no evolution ($\langle V_e/V_a \rangle \approx 0.5$), since the population of intermediate BLs on one hand will gain members from the RBLs, and will lose members to the XBLs as cosmic time increases. In fact, a very recent report (Bade et al. 1998) agrees with this prediction. Bade et al. (1998) have studied a new sample of XBLs selected from RASS. They subdivide their sample into two halves according to the X-ray to optical flux ratio and find that the extremely X-ray–dominated subgroup shows negative evolution, while the subgroup with intermediate SEDs is compatible with no evolution at all. They also find, however, that the extremely X-ray–dominated subgroup has higher X-ray luminosity and redshift than the intermediate subgroup, an effect that does not seem to agree with our model.

5.4. *Emission Line Strength under the* Θ-Λ *Scheme*

The discussion in § 5.1 implicitly treats BLs as AGNs with BELRs and central isotropic sources of thermal ionizing radiation, essentially reducing the differences between BLs and FSRQs. The original definition of a BL Lac object includes the criterion of absent or weak (equivalent width $W_\lambda \lesssim 5$ Å) emission lines (Stickel et al. 1991). This has led most workers in the field to assume that either the gaseous environment near the central engine of BLs is very poor or there is no significant source of ionizing radiation, or both. Additionally, the conviction of a bimodality separating BLs and FSRQs in terms of their emission-line properties had been established. The situation, though, is far from clear and recent results point toward a continuous transition from BLs to FSRQs in terms of their emission-line characteristics. Even in the complete sample of Stickel et al. (1991), the authors identified six out of 34 RBLs that had emission lines violating the equivalent width limit of 5 Å. It is also true that the equivalent width is variablem, and there are objects that change classification depending on the time of observation (Antonucci 1993; Ulrich, Maraschi, & Urry 1997).

The BL PKS 0521−365 (Scarpa, Falomo, & Pian 1995) and the prototype object of this class, BL Lacertae (Vermeulen et al. 1995) have shown emission lines with equivalent widths $W_\lambda \gtrsim 5$ Å. More surprisingly, the X-ray–selected BL Mkn 501, which has recently been detected at TeV energies (Quinn et al. 1996), has shown emission lines in the past (Moles, Masegosa, & del Olmo 1987). Corbett et al. (1996) argue in the case of BL Lacertae that the most plausible way to power the emission lines is through thermal radiation from an accretion disk. The required thermal radiation power does not alter significantly the total observed flux and the object does not show the "big blue bump" component that many radio-loud quasars exhibit.

In a recent study of emission-line luminosities for a sample of HPQs and RBLs, Scarpa & Falomo (1997) find that the line luminosity ranges of HPQs and BLs largely overlap, although RBLs have smaller equivalent widths. Specifically, in Figure 10 of their paper they plot the line luminosity in Mg II versus the continuum luminosity for the sources of their sample, as well as the line that corresponds to the equivalent width limit $W_\lambda = 5$ Å. Their results clearly demonstrate that for any given continuum luminosity the corresponding emission line luminosity does not show any gap separating RBLs and HPQs. If we were to increase the arbitrary 5 Å limit then we would accept as BLs sources that previously have been classified as HPQs. Similarly, lowering the equivalent width limit would shift objects from the BL to the HPQ family. It therefore seems plausible that the gaseous environments of BLs, although poorer than those of the HPQs, may not be qualitatively different from them.

Additional arguments for the presence of ionized gas close to the central engines of BLs come from studies of X-ray and extreme UV (EUV) absorption features in XBLs. Madejski et al. (1991) found in all objects from a sample of five XBLs an absorption feature at an energy of $\sim$650 eV. Königl et al. (1995) studied the X-ray–bright BL PKS 2155−304 with the *Extreme Ultraviolet Explorer* and found an absorption feature between $\sim$75 and $\sim$85 Å. They modeled this feature as absorption resulting from gas

clouds at a distance from the central engine similar to the typical BELR size, moving with a speed $\sim 0.1\ c$. Similar results have been reported recently from EUV observations of the XBL Mkn 421 (Kartje et al. 1997), and X-ray observations of the XBL H1426+428 (Sambruna et al. 1997).

In Figure 6 we plot the synchrotron peak apparent luminosity L_s as a function of the synchrotron peak frequency ν_s for the XBL (*diamonds*) and RBL (*triangles*) samples of Sambruna et al. (1996). The RBLs with emission lines that violate the 5 Å equivalent width criterion are marked with small filled circles. Note that these sources are preferentially low-ν_s, high-L_s objects. We use the scaling relation (eq. [19]) coupled with the accelerating jet model to show that the lack of emission lines in high-ν_s, low-L_s (BL15–BL17) BLs and the existence of emission lines preferentially in low-ν_s, high-L_s (BL13–BL14) BLs can be reconciled with the existence of a scaled-down accretion disk illuminating a BELR.

In Figure 7 we plot the SED for a range of $\Lambda_{\rm kin}$. We assume that the BELR luminosity is proportional to the jet electron kinetic luminosity, and for the purpose of the demonstration we consider a broad line with a full width at half-maximum (FWHM) of 3000 km s^{-1} and with power $L_{\rm BELR} = 0.3\Lambda_{\rm kin}$. The BELR luminosity is shown by the short horizontal line centered at $\nu = 10^{15}$ Hz. As $\Lambda_{\rm kin}$ and $L_{\rm BELR}$ decrease, the synchrotron peak frequency ν_s increases. Although the decrease of $\Lambda_{\rm kin}$ is accompanied by a decrease in the emitted power νL_ν at every frequency, the shift of ν_s toward higher frequencies results in the gradual dominance

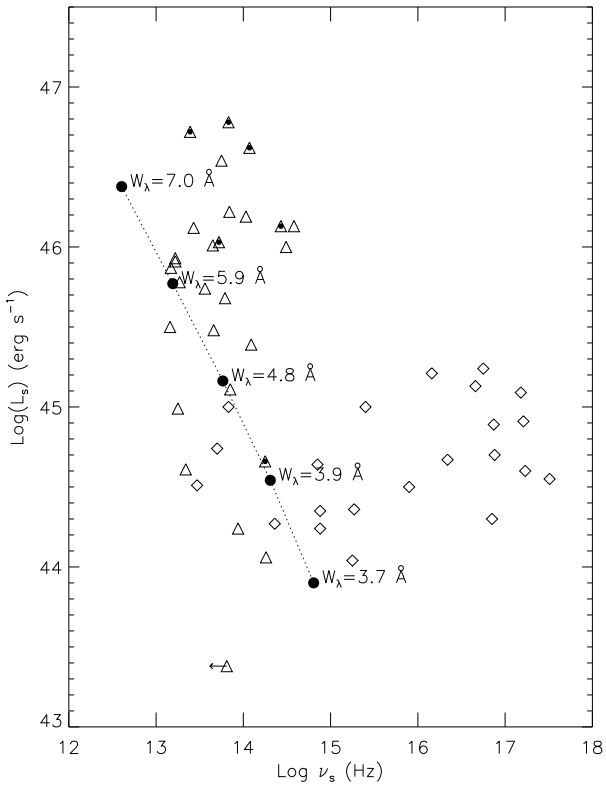

FIG. 6.—Synchrotron apparent peak luminosity L_s as a function of the observed synchrotron peak frequency ν_s for the XBL (*diamonds*) and RBL (*triangles*) samples of Sambruna et al. (1996). Small filled circles mark RBLs with emission lines that violate the 5 Å equivalent width criterion. The bigger filled circles, connected with a dotted line, represent the model points of Fig. 7. The most luminous model source is assigned an arbitrary equivalent width $W_\lambda = 7$ Å, and the variation of the equivalent width W_λ is shown as $\Lambda_{\rm kin}$ and $L_{\rm BELR}$ decrease.

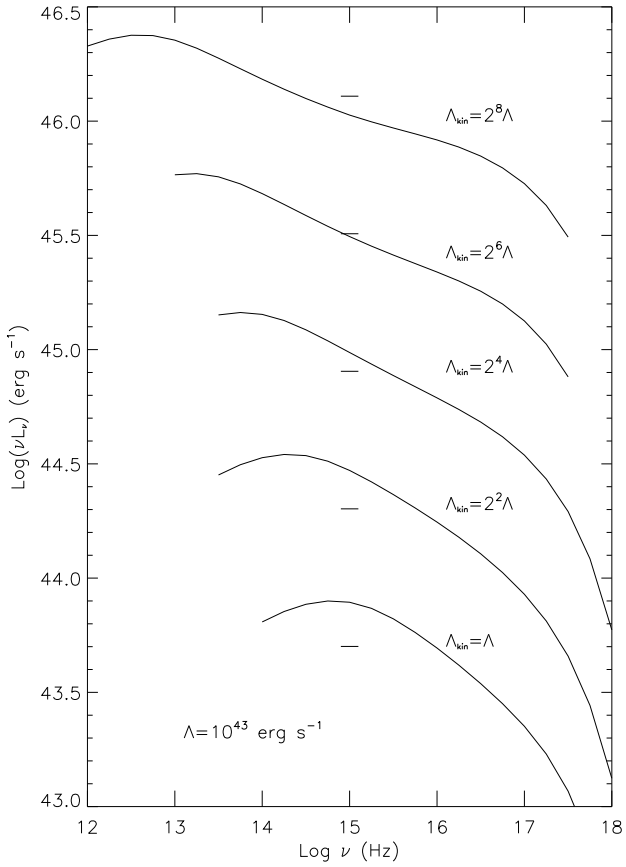

FIG. 7.—SED for a range of jet electron kinetic luminosities. The BELR luminosity, shown by the short horizontal lines, is proportional to the jet electron kinetic luminosity (see § 5.4). The parameters that describe the jet are the same as the parameters describing the family A jets in Table 3, with $\Theta = 3°$.

of the synchrotron emission over the line radiation. In Figure 6 we plot as filled circles the loci of the model for the range of luminosities used in Figure 7. The qualitative behavior of the model is similar to the trends exhibited by the data: as the model points shift to higher values of ν_s and lower values of L_s, the equivalent width W_λ decreases, crossing over to values smaller than 5 Å.

Thus, although the ratio of jet electron kinetic luminosity to BELR luminosity remains the same, the equivalent width of the emission lines decreases as the electron kinetic luminosity of the source decreases. This is again a manifestation of the breakdown in self-similarity described in § 5.2.

6. SUMMARY AND DISCUSSION

The main points of this work are as follows.

1. We verify that an increase in the angle Θ between the line of sight and the jet axis shifts the observed characteristics of the source from the RBL to the XBL class. As has been noted, however (Sambruna, Maraschi, & Urry 1996; Georganopoulos & Marscher 1996), this shift is not enough to explain the range of observed physical parameters in complete BL samples.

2. We propose a new continuous classification scheme for BLs, based on the synchrotron peak frequency ν_s of the SED of a source. This scheme avoids the observationally induced bimodality of the currently used XBL-RBL, or HBL-LBL schemes, and naturally accommodates the newly

discovered (Laurent-Muehleisen 1997; Laurent-Muehleisen et al. 1998; Perlman et al. 1998) intermediate BLs. As can be seen in the results of Sambruna et al. (1996), given the class of a BL, we can infer upper limits to the synchrotron luminosity of the object, the steepness of the spectrum at different frequencies, and the maximum concavity index $\alpha_{ox} - \alpha_X$.

3. Observations suggest that BLs may be characterized by a scaled-down accretion disk and BELR, similar to those found in FSRQs. Based on recent observational results, we propose a self-similar blazar description, according to which the accretion disk luminosity, the broad-line region (BLR) luminosity, and the jet kinetic luminosity scale with the square of the scale size of the jet (eq. [19]). This description leaves invariant all the primary physical parameters such as the pressure and particle and energy densities at the base of the jet.

We propose the Θ-Λ scheme unification scheme: the electron kinetic luminosity, together with the orientation of the jet, determines the observed characteristics of a source. A small range of the physical parameters that describe the jet, together with the Θ-Λ scheme, can reproduce the range of observed BL synchrotron peak frequencies ν_s, which cannot be reproduced solely by orientation effects (Sambruna, Maraschi, & Urry 1996; Georganopoulos & Marscher 1996).

4. The negative evolution of the XBLs can be explained naturally in the context of this self-similarity based scenario. If we start with a random sample of sources, as cosmological time passes, the electron kinetic luminosity decreases, the peak frequency ν_s for each source increases, and the number of sources that would be classified as XBLs increases. We predict that samples of intermediate sources will have a $\langle V_e/V_a \rangle$ value intermediate between those of XBL and RBL samples, as new results have indicated.

5. We show that the existence of emission lines preferably in low-ν_s (BL13–BL14), high-L_s sources, and the lack of lines in higher ν_s, lower L_s objects, is reproduced under a scaling relation (eq. [19]). As both Λ_{kin} and L_{BELR} decrease, ν_s shifts toward the frequency of the emission lines and the nonthermal continuum gradually dominates over the emission line luminosity.

Our discussion of the Θ-Λ scheme has been confined to the BLs, although there are many indications that a common underlying physical mechanism could describe all blazars. Since the luminosity output of FSRQs is dominated in many cases by the γ-ray flux and our simulation does not calculate the inverse Compton energy losses, we cannot at present apply our model to FSRQs. The extended radio luminosity distribution of FSRQs is similar to that of FR II radio galaxies (Maraschi & Rovetti 1994), and the jet magnetic fields tend to be aligned with the jet axes (Cawthorne et al. 1993). BLs, on the other hand, have extended radio luminosity distributions similar to those of FR I radio galaxies (Perlman & Stocke 1993), and the jet magnetic fields tend to be perpendicular to the jet axes (Gabuzda et al. 1992).

Although it may seem as if these differences are enough to separate BLs and FSRQs into two distinct families, there are many observational arguments that support the possibility of a continuous distribution of sources that belong to a single, continuous family. We have already reviewed observations suggesting that a separation of blazars on the basis of the emission line properties may not be justified. The extended radio power distribution for BLs and FSRQs overlap significantly, and the same holds for their parent populations, the FR I and FR II radio galaxies (Maraschi & Rovetti 1994; Padovani 1992). A population of FR II radio galaxies with low-excitation narrow-line spectra, low radio power, and more relaxed radio morphologies (Laing et al. 1994) is indicative of a connection between FR I and FR II sources. Recent VLBI studies (Cawthorne & Gabuzda 1996; Kollgaard et al. 1996a; Gabuzda et al. 1994; Leppänen, Zensus, & Diamond 1995; Kemball, Diamond, & Pauliny-Toth 1996) indicate that the magnetic field orientation does not always follow the previously observed bimodality, and FSRQs with perpendicular and BLs with parallel magnetic field are not rare. Additionally, recent results (Lister & Marscher 1998) from higher frequency (43 GHz) VLBI observations indicate that the magnetic field

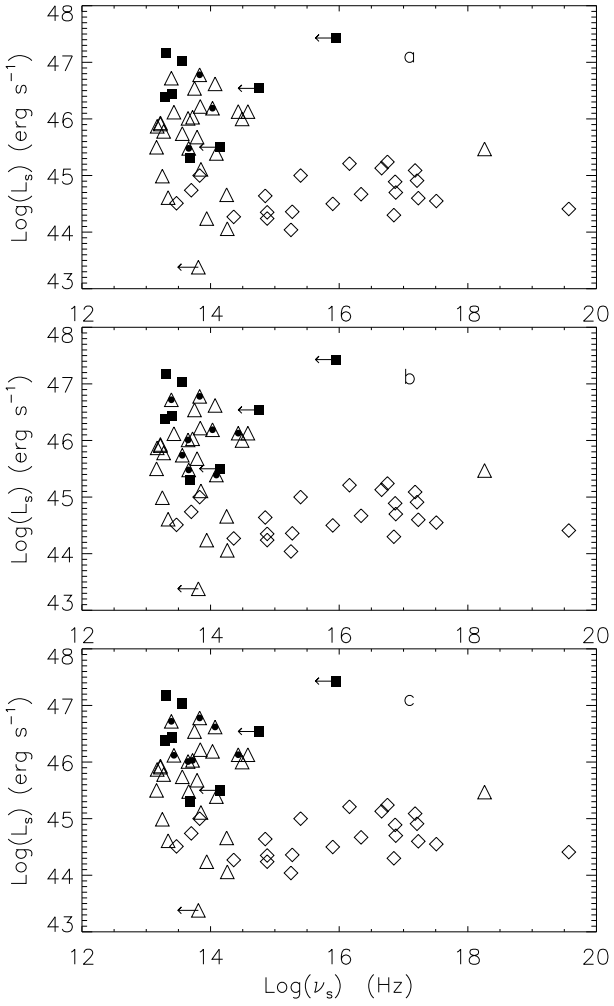

FIG. 8.—Peak synchrotron apparent luminosity vs. observed peak frequency for the two BL samples (see Fig. 6) and the small complete sample of FSRQs (*filled squares*) from the S5 survey (Brunner et al. 1994) used by Sambruna et al. (1996). Small filled circles mark (*a*) RBLs with magnetic field parallel to the jet (0735+178, 1308+326, and 2007+777 from Gabuzda et al. 1994); (*b*) RBLs with FR II–like extended radio characteristics (0235+164, 1308+326, 1538+149, and 1823+568 from Murphy et al. 1993; 0954+658, 1749+701, and 2007+777 from Kollgaard et al. 1992; and 1807+698 from Wrobel & Lind 1990); (*c*) RBLs with emission lines that violate the 5 Å equivalent width criterion (0235+164, 0537–441, 0851+202, 1308+326, and 1749+096 from Stickel et al. 1991; BL Lacertae from Vermeulen et al. 1995).

orientations of both BLs and FSRQs in the radio core region are similar.

In the samples that Sambruna et al. (1996) consider, there are several BLs that have extended radio characteristics that correspond to FR II radio galaxies (Kollgaard et al. 1992; Murphy, Browne, & Perley 1993; Wrobel & Lind 1990), or have longitudinal magnetic fields (Gabuzda et al. 1994). As can be seen in Figure 8, all these BLs are low-ν_s (BL13–BL14), high-L_s objects that occupy a region of the parameter space in the ν_s-L_s diagram similar to that occupied by the FSRQ sample. It therefore seems justifiable to consider that the properties of BLs and FSRQs do not correspond to two distinct physical structures, but, rather, form a continuum.

Since the jets in these sources are relativistic, the angle that a jet forms with the line of sight must be one of the parameters that affects its observed properties. The range of observed luminosities for objects with similar synchrotron peak frequencies ν_s has led us to propose that a second crucial parameter is the electron kinetic luminosity of the jet. Our simulations show that this formulation indeed holds promise for a global understanding of blazars. For further progress, detailed, time-dependent simulations that include in an accurate fashion the relevant physical processes, such as inverse Compton scattering of both jet synchrotron photons and external photons, need to be developed and compared to observations of individual sources and to the statistical properties of complete samples.

This research was supported in part by the NASA Astrophysical Theory Program grant NAG 5-3839.

APPENDIX A

GASDYNAMICS

We describe here the analytical one-dimensional steady flow described by Blandford & Rees (1974). The plasma produced in the vicinity of the central engine is ultrarelativistic in the fluid proper frame (mean total to rest mass ratio per particle $\gamma \gg 1$) and remains in the ultrarelativistic regime as it flows downstream. The flow is considered adiabatic and quasi-spherically symmetric; i.e., the jet is confined to a cone. The pressure profile is parameterized by a power law,

$$p(z) = p_0\left(\frac{z}{z_0}\right)^{-a}, \tag{A1}$$

where the z-axis is the symmetry axis of the system, z_0 is the distance of the flow stagnation point (bulk motion Lorentz factor $\Gamma = 1$) from a fiducial point where the pressure mathematically becomes infinite, p_0 is the pressure at z_0, and a is the exponent that describes how fast the pressure drops ($a \geq 0$) as we move away from the central engine along the z-axis. Note that $z = 0$ at the fiducial point and not at the central engine. The jet is characterized by a constant power,

$$\Lambda_t = \Gamma^2 \beta w c A , \tag{A2}$$

where β is the jet velocity in units of c, w is the enthalpy density in the fluid frame, and A is the cross section of the jet at a given z. For a relativistic gas, $w = (4/3)e$, where e is the comoving energy density of the plasma.

One way to ensure that the flow is adiabatic is to assume that a significant portion of the energy is carried by relativistic protons that have essentially no radiative losses. Alternatively, we confine our study to EED with $s > 2$, which corresponds to most of the energy being near the low-energy cutoff of the EED. Since the low-energy electrons have small radiative losses, such a flow is approximately adiabatic. We use the first description,

$$e = e_{\rm el} + e_p,\ e_{\rm el} = ke ,\qquad e_p = (1-k)e ,\qquad 0 < k < 1 , \tag{A3}$$

where

$$e_{\rm el} = \int_{\gamma_{\rm min}}^{\gamma_{\rm max}} \gamma N_\star \gamma^{-s}\, d\gamma = \frac{N_\star}{2-s}\left(\gamma_{\rm max}^{2-s} - \gamma_{\rm min}^{2-s}\right) \tag{A4}$$

is the electron energy density and e_p is the proton energy density in the comoving frame. Assuming equipartition between the electron and proton energy density, we set $k = 0.5$ (the actual requirement is $k \lesssim 0.5$). This ensures that one-half of the energy is in protons that do not radiate, and therefore our adiabatic approximation is reasonable. Therefore, the electron kinetic luminosity $\Lambda_{\rm kin}$ is

$$\Lambda_{\rm kin} = k\Lambda_t = \Lambda_t/2 . \tag{A5}$$

The cross section of the jet is minimized at the sonic point [$\Gamma_\star = (3/2)^{1/2}$], which is characterized by a pressure

$$p_\star = \tfrac{4}{9} P_0 , \tag{A6}$$

a cross sectional radius

$$r_\star = 2^{1/4}\left(\frac{3}{2}\right)^{3/4}\left(\frac{\Lambda_{\rm kin}}{4\pi c p_0}\right)^{1/2}, \tag{A7}$$

and a distance from the fiducial point

$$z_\star = z_0\left(\tfrac{9}{4}\right)^{1/a} . \tag{A8}$$

The cross-sectional radius of the jet as a function of z is given by

$$r(z) = r_\star \left(\frac{z}{z_\star}\right)^{3\epsilon/2} \left[3\left(\frac{z}{z_\star}\right)^{2\epsilon} - 2\right]^{-1/4}, \tag{A9}$$

and the bulk Lorentz factor of the flow Γ is given by

$$\Gamma(z) = \Gamma_\star \left(\frac{z}{z_\star}\right)^{\epsilon}. \tag{A10}$$

The exponent ϵ determines how fast the jet opens and accelerates and is determined solely by the steepness of the external pressure gradient, $\epsilon = a/4$. For $z \gg z_\star$, $r \propto z^\epsilon$.

APPENDIX B

THOMSON LOSSES

Our treatment of electron losses does not consider the Thomson losses due to the radiation from an accretion disk. If z_1 is the distance of the fiducial point used in the flow description, the distance of the base of the jet from the central engine is $z_{\rm base} = z_1 + z_\star$. The synchrotron losses will be greater than the Thomson losses if the accretion disk photon energy density in the comoving frame at the base of the jet is greater than the comoving magnetic field energy density.

As given in Dermer & Schlickeiser (1994), the comoving photon energy density $u_{\rm acc}$ at distance z from the central engine due to a pointlike accretion disk is

$$u_{\rm acc} = \frac{L_{\rm acc}}{4\pi z^2 c \Gamma_\star^2 (1 + \beta_\star)^2}, \tag{B1}$$

where $L_{\rm acc}$ is the accretion disk luminosity, and $\Gamma_\star$ and $\beta_\star$ describe the jet flow at the base of the jet. Requiring $u_{\rm acc} < B_\star^2/(8\pi)$, we obtain

$$z_{\rm base} > z_{\rm min} = (2/3)^{1/2} 10^{17} L_{44}^{1/2} B_\star^{-1} \Gamma_\star^{-1} (1 + \beta_\star)^{-1} \text{ cm}, \tag{B2}$$

where L_{44} is the accretion disk luminosity in units of 10^{44} ergs s^{-1}. In this work we assume that the fiducial point is adequately far from the central engine so that relation B2 is satisfied.

REFERENCES

Antonucci, R. 1993, ARA&A, 31, 473
Appl, S. 1996, in ASP Conf. Proc. 110, Energy Transport in Radio Galaxies and Quasars, ed. P. E. Hardee, A. H. Bridle, & J. A. Zensus (San Francisco: ASP), 129
Bade, N., Beckmann, V., Douglas, N. G., Barthel, P. D., Engels, D., Cordis, L., Nass, P., & Voges, W. 1998, A&A, in press
Blandford, R. D., & Payne D. G. 1982, MNRAS, 199, 883
Blandford, R. D., & Rees, M. J. 1974, MNRAS, 169, 395
———. 1978, in Pittsburgh Conference on BL Lac Objects, ed. A. N. Wolfe (Pittsburgh: Univ. Pittsburgh Press), 328
Bloom, S. D., & Marscher, A. P. 1996, ApJ, 461, 657
Brunner, H., Lamer, G., Worrall, D. M., & Staubert, R. 1994, A&A, 287, 436
Buckley, J. H., et al. 1996, ApJ, 472, L9
Cawthorne, T. V., & Gabuzda, D. C. 1996, MNRAS, 278, 861
Cawthorne, T. V., Wardle, J. F. C., Roberts, D. H., & Gabuzda, D. C. 1993, ApJ, 416, 519
Celotti, A., Padovani, P., & Ghisellini, G. 1997, MNRAS, 286, 415
Corbett, E. A., Robinson, A., Axon, D. J., Hough, J. H., Jeffries, R. D., Thurston, M. R., & Young, S. 1996, MNRAS, 281, 737
Dermer, C. D. 1995, ApJ, 446, L63
Dermer, C. D., & Schlickeiser, R. 1993, ApJ, 416, 484
———. 1994, ApJS, 90, 945
Dondi, L., & Ghisellini, G. 1995, MNRAS, 273, 583
Edelson, R., et al. 1995, ApJ, 438, 120
Fanaroff, B. L., & Riley, J. M. 1974, MNRAS, 167, 31
Fossati, G., Celotti, A., Ghisellini, G., & Maraschi, L. 1997, MNRAS, 289, 136
Fossati, G., Maraschi, L., Celotti, A., Comastri, A., & Ghisellini, G. 1998, MNRAS, submitted
Gabuzda, D. C., Cawthorne, T. V., Roberts, D. H., & Wardle, J. F. C. 1992, ApJ, 388, 40
Gabuzda, D. C., Mullan, C. M., Cawthorne, T. V., Wardle, J. F. C., & Roberts, D. H. 1994, ApJ, 435, 140
Gear, W. K. 1992, MNRAS, 264, 919
Georganopoulos, M., & Marscher, A. P. 1996, in ASP Conf. Proc. 110, Blazar Continuum Variability, ed. H. R. Miller, J. R. Webb, & J. C. Noble (San Francisco: ASP), 262
Ghisellini, G., & Maraschi, L. 1989, ApJ, 340, 181
Gómez, J. L., Martí, J. M., Marscher, A. P., Ibáñez, J. M., & Alberdi, A. 1997, ApJ, 482, L33
Jannuzi, B. T., Smith, P. S., & Elston, R. 1994, ApJ, 428, 130
Kartje, J. F., Königl, A., Hwang, C.-Y., & Bowyer, S. 1997, ApJ, 474, 630
Kaspi, S., Smith, P. S., Maoz, D., Netzer, H., & Januzzi, B. T. 1996, ApJ, 471, L75
Kemball, A. J., Diamond, P. J., & Pauliny-Toth, I. I. K. 1996, ApJ, 464, L55
Kirk, J. G. 1997, in Relativistic Jets in AGNs, ed. M. Ostrowski, M. Sikora, G. Madejski, & M. C. Begelman (Cracow: Poligrafia Inspektoratu), 328
Kollgaard, R. I., Gabuzda, D. C., & Feigelson E. D. 1996a, ApJ, 460, 174
Kollgaard, R. I., Palma, C., Laurent-Muehleisen, S. A., & Feigelson E. D. 1996b, ApJ, 465, 115
Kollgaard, R. I., Wardle, J. F. C., Roberts, D. H., & Gabuzda, D. C. 1992, AJ, 104, 1687
Königl, A., Kartje, J. F., Bowyer, S., Kanh, S. M., & Hwang, C.-Y. 1995, ApJ, 446, 598
Koratkar, A., Pian, E., Urry, C. M., & Pesce, J. E. 1998, ApJ, 492, 173
Laing, R. A., Jenkins, C. R., Wall, J.V., & Unger, S. W. 1995, in ASP Conf. Proc. 54, The Physics of Active Galaxies, ed. G. V. Bicknell, M. A. Dopita, & P. J. Quinn (San Francisco: ASP), 201
Lamer, G., Brunner, H., & Staubert, R. 1996, A&A, 311, 384
Laurent-Muehleisen, S. A. 1997, PASP, 109, 341
Laurent-Muehleisen, S. A., Becker, R. H., Brinkmann, W., Gregg, M. D., Kollgaard, R. I., McMahon, R. G., & White, R. L. 1998, BAAS, 29, 1241
Ledden, J. E., & O'Dell, S. L. 1985, ApJ, 298, 630
Leppänen, K. J., Zensus, J. A., & Diamond, P. J. 1995, AJ, 110, 2479
Lister, M., & Marscher, A. P. 1998, ApJ, submitted
Macomb, D. J., et al. 1995, ApJ, 449, L99
Madejski, G. M., Mushotzky, R. F., Weaver, K. A., & Arnaud, K. A. 1991, ApJ, 370, 198
Maraschi, L., Ghisellini, G., Tanzi, E. G., & Treves, A. 1986, ApJ, 310, 325

Maraschi, L., & Rovetti, F. 1994, ApJ, 436, 79
Marscher, A. P. 1980, ApJ, 235, 386
Marscher, A. P., & Bloom, S. D. 1994, in AIP Conf. Proc. 304, The Second Compton Symposium, ed. C. E. Fichtel, N. Gehrels, & J. P. Norris (New York: AIP), 573
Moles, M., Masegosa, J., & del Olmo, A. 1987, AJ, 94, 1143
Morris, S. L., Stocke, J. T., Gioia, I. M., Schild, R. E., Wolter, A., Maccacaro, T., & Della Ceca, R. 1991, ApJ, 380, 49
Murphy, D. W., Browne, I. W. A., & Perley, R. A. 1993, MNRAS, 264, 298
Ouyed, R., Pudritz, R. E., & Stone, J. M. 1997, Nature, 385, 409
Pacholczyk, A. G. 1970, Radio Astrophysics (San Francisco: Freeman)
Padovani, P. 1992, MNRAS, 257, 404
Padovani, P., & Giommi, P. 1995, ApJ, 444, 567
Padovani, P., Giommi, P., & Fiore, F. 1996, MNRAS, 279, 536
Padovani, P., & Urry, C. M. 1990, ApJ, 356, 75
Perlman, E. S., & Stocke, J. T. 1993, ApJ, 406, 430
Perlman, E. S., Stocke, J. T., Wang, Q. D., & Morris, S. L. 1996, ApJ, 456, 451
Perlman, E. S., Padovani, P., Giommi, P., & Sambruna, R., Laurence, R. J., Tzioumis, A., & Reynolds, J. 1998, AJ, 115, 1253
Pian, E., et al. 1998, ApJ, 492, L17
Quinn, J., et al. 1996, ApJ, 456, L83
Rawlings, S. G., & Saunders, R. D. E. 1991, Nature, 349, 138
Rees, M. J., Begelman, M. C., Blandford, R. D., & Phinney, E. S. 1982, Nature, 295, 17
Reynolds, S. P. 1982, ApJ, 256, 13
Rybicki, G. R., & Lightman, A. P. 1979, Radiative Processes in Astrophysics (New York: Wiley)
Sambruna, R. M., George, I. M., Madejski, G., Urry, C. M., Turner, T. J., Weaver, K. A., Maraschi, L., & Treves, A. 1997, ApJ, 483, 774
Sambruna, R. M., Maraschi, L., & Urry, C. M. 1996, ApJ, 463, 444
Scarpa, R., & Falomo, R. 1997, A&A, 325, 109
Scarpa, R., Falomo, R., & Pian, E. 1995, A&A, 303, 730
Sikora, M., Begelman, M. C., & Rees, M. J. 1994, ApJ, 421, 153
Stickel, M., Padovani, P., Urry, C. M., Fried, J. W., & Kühr, H. 1991, ApJ, 374, 431
Ulrich, M.-H., Maraschi, L., & Urry, C. 1997, ARA&A, 35, 445
Urry, C. M., & Padovani, P. 1995, PASP, 107, 803
Urry, C. M., Padovani, P., & Stickel, M. 1991, ApJ, 382, 501
Urry, C. M., et al. 1997, ApJ, 486, 799
Vermeulen, R. C., Ogle, P. M., Tran, H. D., Browne, I. W. A., Cohen, M. H., Readhead, A. C. S., & Taylor, G. B. 1995, ApJ, 452, L5
Vestrand, W. T., Stacy, J. G., & Sreekumar, P. 1995, ApJ, 454, L96
von Montigny, C., et al. 1995, ApJ, 440, 525
Wandel, A. 1997, ApJ, 490, L131
Wrobel, J. M., & Lind, K. R. 1990, ApJ, 348, 135